Journal of Materials Science: Materials in Electronics (2020) 31:6900–6909
https://doi.org/10.1007/s10854-020-03252-7

Synthesis, optical and optoelectrical analysis of the Cu_2CoSnS_4 thin films as absorber layer for thin-film solar cells

H. Y. S. Al-Zahrani[1]

Received: 12 January 2020 / Accepted: 13 March 2020 / Published online: 26 March 2020

Abstract

In this work, the optical and optoelectrical characterizations of the quaternary kesterite Cu_2CoSnS_4 ($CCTS_4$) thin films were studied. The polycrystalline $CCTS_4$ films have prepared by the spray pyrolysis method at four different thicknesses (160 nm, 230 nm, 297 nm and 345 nm). The X-ray diffraction charts demonstrated that the as-prepared $CCTS_4$ films have a polycrystalline nature with tetragonal single phase. The linear optical parameters of the $CCTS_4$ films were computed by finding the transmission and reflection data. The magnitudes of the absorption coefficient for the $CCTS_4$ films were high in the order of 10^5 cm^{-1} while the energy gap of the $CCTS_4$ films has been reduced from 1.41 to 1.12 eV by raising the film thickness. The optical conductivity and the Urbach energy of the $CCTS_4$ films were computed from the absorption coefficient data. In addition, the nonlinear optical parameters represented in the nonlinear refractive index n_2 and the third-order nonlinear optical susceptibility $\chi^{(3)}$ of the $CCTS_4$ films were boosted with rising up the film thickness.

1 Introduction

In recent years, kesterite materials are gaining importance in the different articles due to its stable, earth-abundant, nontoxic and have excellent electrical and optical properties. All of these properties make the kesterite materials capable of being good compotators to conventional materials like CdTe, GaAs materials [1–3]. The privilege of the kesterite materials is by virtue of their stability after the preparation for a long time without revealing any mark for degradation. Such characteristics make these materials as good candidates for different applications like optical devices and photovoltaic devices [4, 5]. Recently, the articles concentrated on a different kesterite materials like Cu_2ZnSnS_4, Cu_2NiSnS_4, Cu_2CoSnS_4, and Cu_2FeSnS_4 due to they displayed a high absorption coefficient, p-type conductivity and narrow bandgap. So these materials act as good absorber layers in thin-film solar cells [6, 7]. These kesterite thin films demonstrated high solar efficiency in various articles. The efficiency of the CZTS solar cell is 5.1% by the spray pyrolysis technique [8] and reaches to 9.6% via the thermal evaporation process [9]. Moreover, the Cu_2NiSnS_4 thin films display excellent electrical properties in the Ag/*n*-Si/Cu_2NiSnS_4/Au heterojunction which demonstrate a solar efficiency of about 11.34% [10]. The previous articles displayed that the Cu_2CoSnS_4 ($CCTS_4$) thin films demonstrate p-type conductivity, and narrow energy gap so they suitable to be a good absorber layer for thin-film solar cells [11]. The $CCTS_4$ films have been prepared by various processes like spin coating [12], spray pyrolysis technique [13] and electrodeposition [14]. The previous studies on the Cu_2CoSnS_4 films were concentrated on the structural, current–voltage and energy gap studies. Beraich et.al present the X-ray diffraction, Raman spectroscopy and energy gap studies of the Cu_2CoSnS_4 films [14]. El Radaf et.al present the electrical and photovoltaic properties of the Al/n-Si/ Cu_2CoSnS_4/Au heterojunction which demonstrates a solar efficiency of 6.17% [15]. The previous studies displayed that, there are no articles reported the optoelectrical, dispersion and nonlinear optical properties of the $CCTS_4$ films. So this work focused on studying the optoelectrical, linear/nonlinear optical properties of $CCTS_4$ films that are deposited by utilizing the spray pyrolysis technique.

✉ H. Y. S. Al-Zahrani
dr.alzahrani14@gmail.com; hyalzahrani@kau.edu.sa

[1] Physics Department, Faculty of Science & Arts, King Abdulaziz University, Rabigh, Saudi Arabia

2 Experimental details

$CCTS_4$ thin films were fabricated successfully using an inexpensive spray pyrolysis technique via the reaction between high purity copper chloride, cobalt chloride, tin chloride and thiourea according to the present molarity 0.1 M copper chloride, 0.05 M cobalt chloride, 0.05 M tin chloride and 0.2 M thiourea $SC(NH_2)_2$. A double distilled water was used for solution preparation. The $CCTS_4$ solution was magnetically stirred at 50 °C for 1 h to get a uniform brown solution. The $CCTS_4$ solution was sprayed above the glass substrate via the spray pyrolysis technique according to the following conditions: the solution flow rate equal 20 ml/min, the substrate temperature equal 300 °C, the pressure of air equal 3 at and the distance between the nozzle and substrate adjusted to be 30 cm. $CCTS_4$ thin-film thickness was measured via an alpha step D 500 stylus profilometer. Finally, thickness magnitudes of $CCTS_4$ films were (160 nm, 230 nm, 297 nm and 345 nm).

In this work, the structural and surface morphology characterizations of the $CCTS_4$ films were researched via Philips X' pert diffractometer, and the field emission scanning electron microscope (FE-SEM, Quanta FEG 250, and FEI, USA), respectively. The optical investigations like the optoelectrical, linear/nonlinear optical calculations of the $CCTS_4$ films have been investigated by collecting the transmittance and reflectance data of the $CCTS_4$ films using a spectrophotometer (kind JASCO Corp., V-570).

3 Results and discussions

3.1 Structural study

The crystal structure of the $CCTS_4$ thin films was checked by the X-ray diffraction instrument (kind X'Pert) with CuK_α radiation. The results of the XRD for $CCTS_4$ thin films were presented in Fig. 1. The analysis of this figure displayed that the sprayed $CCTS_4$ films are polycrystalline and the indexed planes of the polycrystalline $CCTS_4$ films were matched with the standard data JCPDS No. 26-0513 which belong to the tetragonal crystal system. In addition, the diffraction peaks of this pattern were positioned at 28.49°, 48.36° and 57.31° according to (112), (204) and (312) planes, respectively. Moreover, the structure constants of the polycrystalline $CCTS_4$ films represented in the strain function (ε), the crystallite size (D), the number of crystallites per unit surface area N_C and the dislocation density (δ) were computed according to the below Scherer formulas [16–19]:

$$D = \frac{0.9\lambda}{\beta\cos\theta} \tag{1}$$

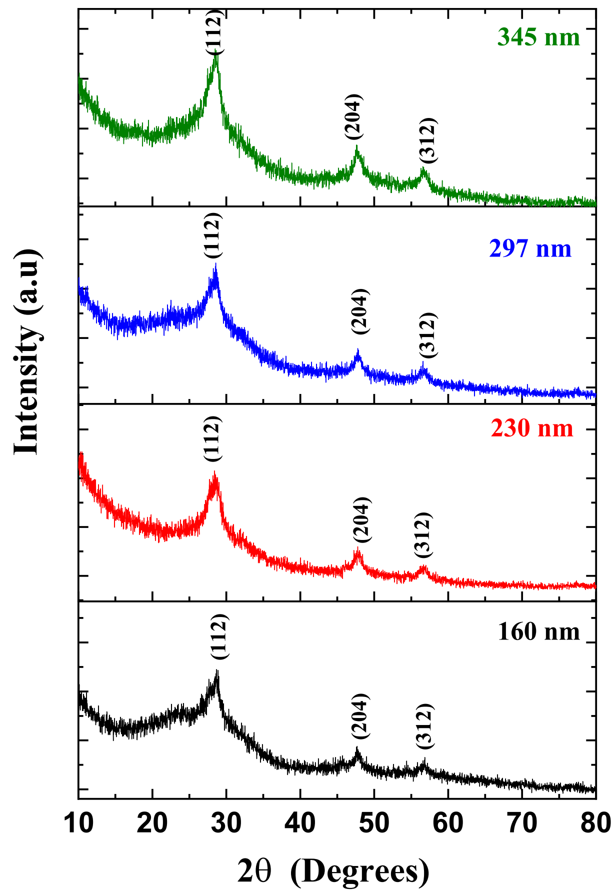

Fig. 1 X-ray diffraction patterns of the $CCTS_4$ thin films deposited at a different thickness (160 nm, 230 nm, 297 nm and 345 nm)

$$\delta = \frac{1}{D^2} \tag{2}$$

$$N_C = \frac{t}{D^3} \tag{3}$$

$$\varepsilon_s = \frac{\beta\cos(\theta)}{4} \tag{4}$$

where $\beta, \theta, \varepsilon, t$ denote the experimental full width at the half maximum (FWHM), the Bragg diffraction angle, the lattice strain and the film thickness, respectively.

Table 1 presented the computed values of D, δ, N_C, and ε_s for the $CCTS_4$ thin films. The results in Table1 demonstrated that the raising of film thickness for the $CCTS_4$ thin films accompanied with a rise in the crystallites size (D). This behavior related to increasing the film thickness leads to coalesce of the crystallites with each other and hence improving the crystallinity of films which led to an increase in the crystallite size D.

Also, the raising of film thickness for the $CCTS_4$ thin films accompanied with a reduction in the magnitudes of the

Table 1 The structure parameters of the sprayed $CCTS_4$ thin films

Thickness (nm)	D (nm)	$\varepsilon \times 10^{-4}$	$\delta \times 10^{-4}$ $(nm)^{-2}$	$N \times 10^{-3}$ (line/nm^3)
160	37	9.36	7.30	3.15
230	43	8.06	5.41	2.89
297	51	6.79	3.84	2.23
345	59	5.87	2.87	1.67

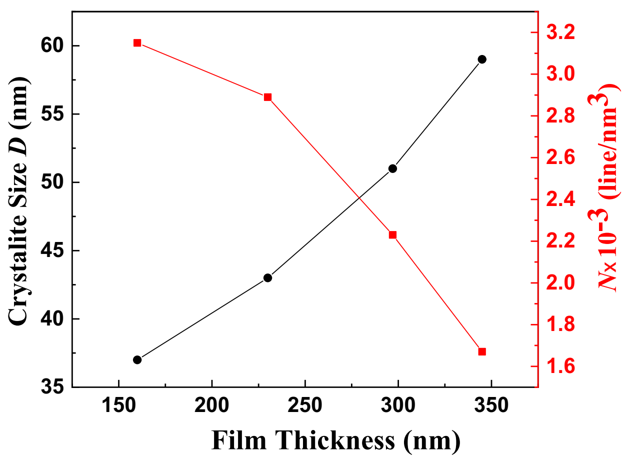

Fig. 2 The crystallite size and the dislocation density as a function of the film thickness for the $CCTS_4$ thin films

dislocation density δ, number of crystallites per unit surface area N_C and the strain function (ε) of the $CCTS_4$ thin films. This behavior due to the δ, N_C, and ε_s is inversely proportional to the crystallite size. So, when the crystalline state of a material depends on crystallite sizes, D; where if D has increased the crystallinity of the material increases. Thus, δ, N_C, and ε_s in the material decreases.

Figure 2 depicted the variation of the crystallites size (D) and the number of crystallites per unit surface area N_C with the thickness of the $CCTS_4$ films. The analysis of this figure displayed that the rise of the film thickness leads to the rise of the values of crystallites size (D) and reduces the magnitudes of the number of crystallites per unit surface area N_C. The EDAX analysis of the $CCTS_4$ thin film synthesized at 345 nm was given in Fig. 3 as a representative example.

The high-resolution SEM micrograph of the $CCTS_4$ thin film synthesized at different thicknesses (160 nm, 230 nm, 297 nm and 345 nm) were illustrated in Fig. 3 and displayed that the $CCTS_4$ films have a uniform and homogeneous surface. Moreover, the EDAX data of the $CCTS_4$ films have been presented in Table 2 which presents the constituents' ratio of the elements forming the studied films. The EDAX analysis and the EDAX graph confirm the existence of copper, cobalt, tin and sulfur in the as-deposited $CCTS_4$ thin films. In addition, the atomic percentage of Cu, Co, Sn and S in the as-deposited $CCTS_4$ films is close to 2:1:1:4 so the $CCTS_4$ films are nearly stoichiometric.

3.2 Linear optical properties

3.2.1 Transmittance and reflectance spectra

In this study, the optical properties of the sprayed $CCTS_4$ films with different thicknesses (160 nm, 230 nm, 297 nm and 345 nm) were investigated via recording optical transmittance and reflectance data in view of incident wavelength λ alteration in the domain of (400–2500 nm). Figure 4a, b present the transmittance and reflectance spectra of the $CCTS_4$ films. It is observed from these curves that the values of reflection for the $CCTS_4$ films were boosted by enlarging the film thickness while the transmittance magnitudes have a reverse manner.

3.2.2 Absorption coefficient and absorption index

The recording of both transmittance and reflectance data of the $CCTS_4$ films helped us in estimating the magnitudes of the absorption coefficient α according to the relation [20, 21]:

$$\alpha = \frac{1}{d}\ln\left[\frac{(1-R)^2}{2T} + \left(\frac{(1-R)^4}{4T^2} + R^2\right)^{1/2}\right] \quad (5)$$

Here d presents the thickness value.

Figure 5a depicts the variation of the absorption coefficient for the $CCTS_4$ films with wavelength. From this plot, it can be seen that the absorption coefficient of the $CCTS_4$ films was increased with the rise of the film thickness. Also, all films revealed high values of the absorption coefficient.

The absorption index (k) of the $CCTS_4$ thin films synthesized at different thicknesses (160 nm, 230 nm, 297 nm and 345 nm) was calculated via the formula [22, 23]:

$$K = \frac{\alpha\lambda}{4\pi} \quad (6)$$

The absorption index dependence on wavelength for the $CCTS_4$ films is given in Fig. 5b. It is seen from this plot that the magnitude of k rises up with increasing the film thickness.

3.2.3 Energy gap and Urbach energy evaluation

The energy gap values for the $CCTS_4$ films were determined using Tauc's equation [24, 25]:

$$\alpha h\nu = B\left(h\nu - E_g\right)^P \quad (7)$$

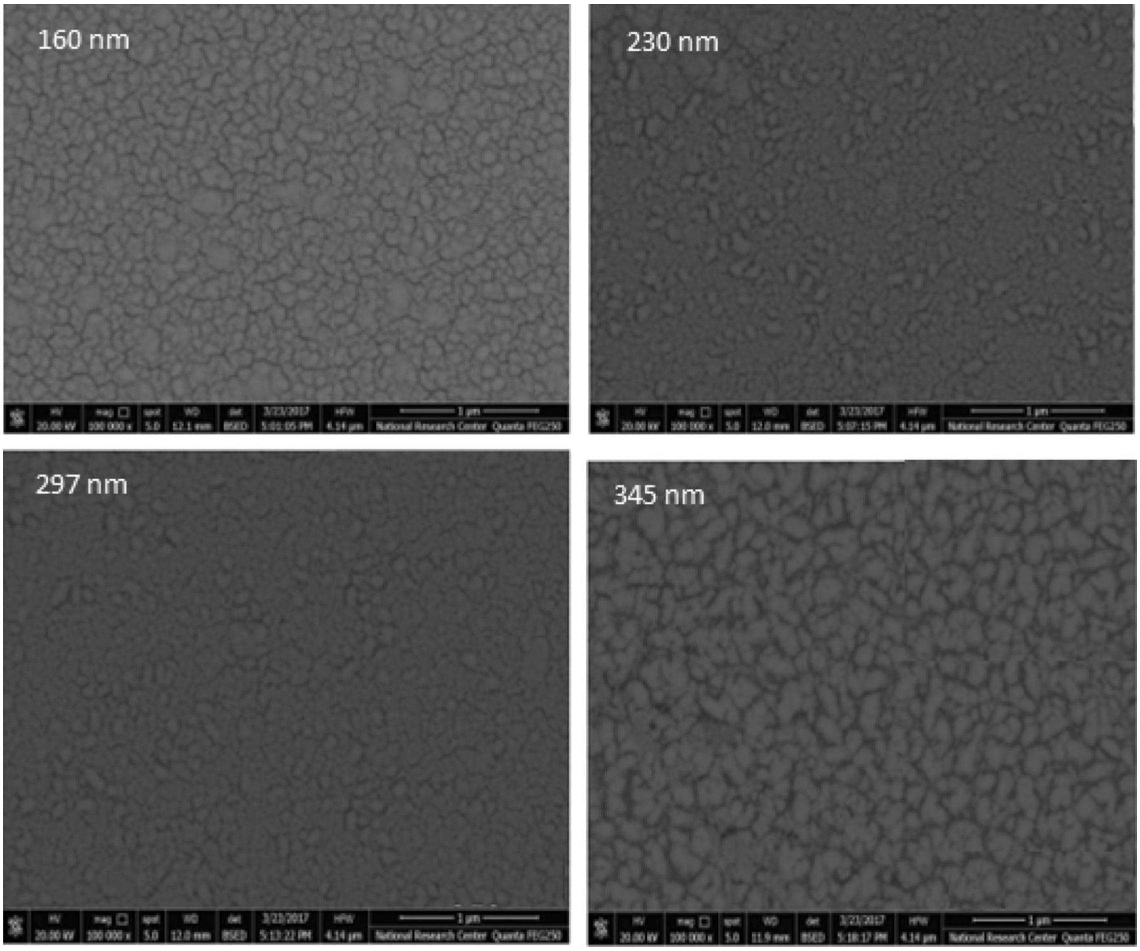

Fig. 3 The SEM micrograph of the $CCTS_4$ film deposited at a different thickness (160 nm, 230 nm, 297 nm and 345 nm)

Table 2 The EDAX data for the $CCTS_4$ thin films

Film thickness (nm)	Si (%)	Cu (%)	Co (%)	Sn (%)	S (%)
160	21.65	20.83	9.32	9.63	38.57
230	20.25	20.17	10.01	9.14	40.43
297	18.48	19.86	9.47	10.87	41.32
345	17.96	18.95	10.39	10.41	42.29

In this equation, p is an important factor that detects the kind of the optical transition where the p value may be equal 1/2, 2 for direct allowed, indirect allowed transitions, respectively. Also, B denotes a band tailing parameter.

The fits for different values of p factor have been examined and the best fit was obtained at p equal 1/2. Figure 6 implies the alteration of $(\alpha h\nu)^2$ due to the variation in photon energy ($h\nu$) for the $CCTS_4$ films. This plot illustrated the direct energy gap for the $CCTS_4$ thin films and the bandgap values were evaluated by extending this straight line of the curve to intercept x-axis at zero $(\alpha h\nu)^2$. Table 3 presented the direct energy gap values for the $CCTS_4$ thin films and these values were lowered from 1.41 to 1.12 eV by enlarging the film thickness. The redshift in the absorption edge with the increase of the thickness comes out from the increase in the grain size that accompanied by boosting the disorders and defects, number localized states in the gap which leads to extending the band tail and thus increasing the Urbach's energy [26, 27]. In addition, Table 4 presents the E_g values for different kesterite thin films like Cu_2CoSnS_4, Cu_2ZnSnS_4, Cu_2CdSnS_4, Cu_2NiSnS_4, Cu_2FeSnS_4 thin films [28–31]. It is noted from this table that, our results in a good agreement with the values recorded by Banavoth, et.al [32]. Moreover, the Urbach's energy E_u of the $CCTS_4$ films was computed via studding the relation between ln (α) and the photon energy ($h\nu$) according to the Urbach formula [33, 34]:

$$\alpha = \alpha_o \exp\left(h\upsilon/E_u\right) \tag{8}$$

Figure 7a illustrates the plotting ln (α) against $h\nu$ for the $CCTS_4$ films with different thicknesses (160 nm, 230 nm, 297 nm and 345 nm). It is observed from this plot that the

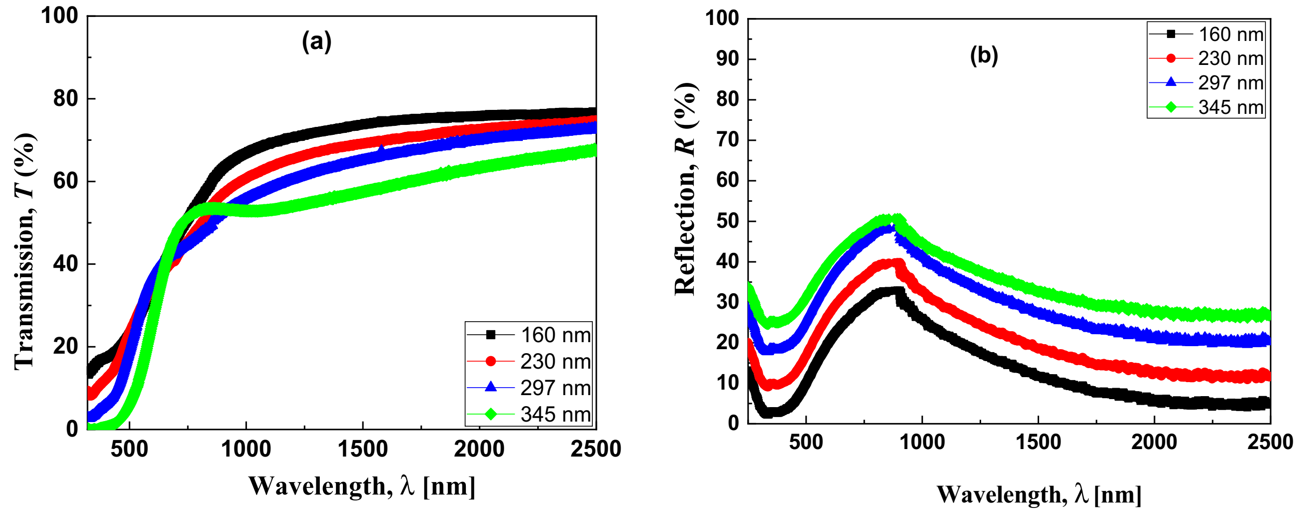

Fig. 4 **a** The transmittance spectra of the $CCTS_4$ films under investigations, **b** the reflectance spectra of the $CCTS_4$ films under investigations

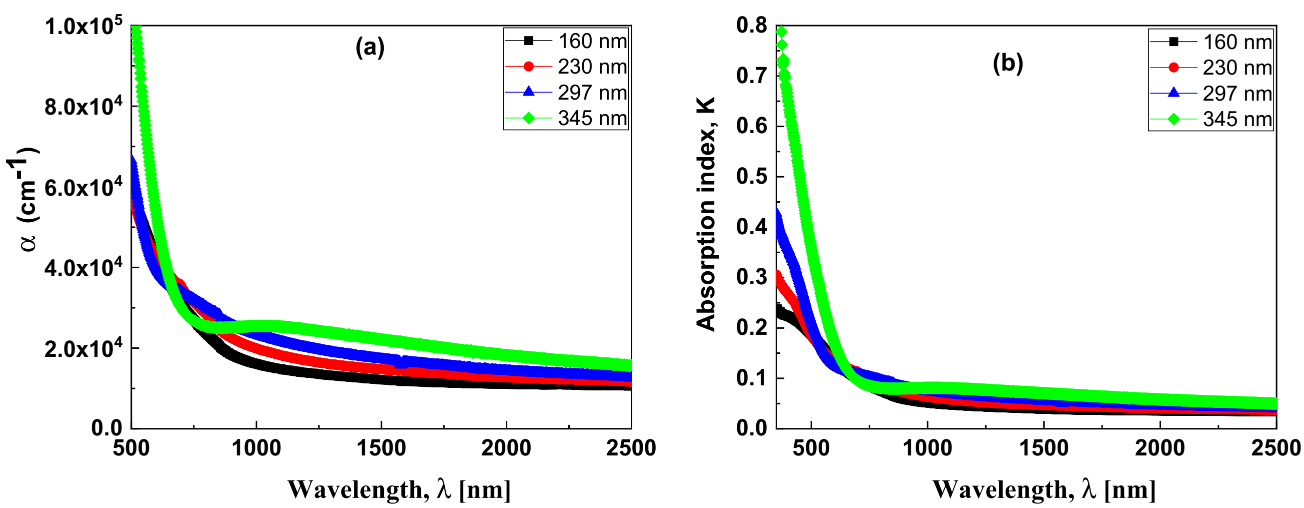

Fig. 5 **a** The absorption coefficient as a function of wavelength for the $CCTS_4$ thin films, **b** The absorption index K as a function of wavelength for the sprayed $CCTS_4$ films

magnitude of Urbach energy E_u of the $CCTS_4$ thin films increased with the rise of the film thickness. The computed values of the E_u for the $CCTS_4$ films were recorded in Table 3.

3.2.4 Refractive index and dispersion analysis

The refractive index, n of the sprayed $CCTS_4$ films synthesized at various thicknesses (160 nm, 230 nm, 297 nm and 345 nm) can be evaluated by exploiting the magnitudes of the reflectance (R) and absorption index (k) according to Fresnel formula [35, 36]:

$$n = \frac{(1+R)}{(1-R)} + \left(\frac{4R}{(1-R)^2} - K^2\right)^{\frac{1}{2}} \quad (9)$$

Figure 7b depicts the impact of film thickness on the refractive of the sprayed $CCTS_4$ films. It is observed that by boosting the film thickness, the refractive index rises up. This behavior related to the rising of the free carrier concentration with rising the film thickness [37].

The dispersion parameters of the $CCTS_4$ films were discussed in view of Wemple–DiDomenico model according to the equation [38]:

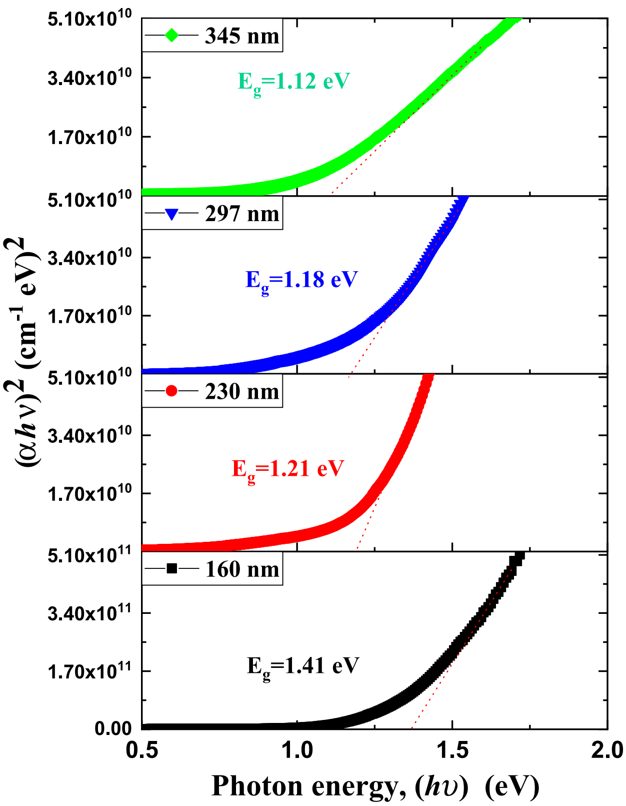

Fig. 6 Plot of $(\alpha h\nu)^2$ versus the photon energy $h\nu$ for the $CCTS_4$ thin films

$$n^2(h\nu) = 1 + \frac{E_d E_o}{\left(E_o^2 - (h\nu)^2\right)} \quad (10)$$

Here $\hbar\upsilon$ displays photon energy.

The E_o and E_d values for the $CCTS_4$ films were extracted from slopes $(E_o E_d)^{-1}$ and intercepts (E_o/E_d) of the plot $(n^2 - 1)^{-1}$ against the $(\hbar\upsilon)^2$ as shown in Fig. 8a. By utilizing E_o and E_d, the oscillation strength parameter has been calculated using the expression, $f = E_0 E_d$. The values of the oscillation strength have been reduced by rising up the film thickness.

The dependences of dispersion energy, as well as the oscillation energy on the variation of film thickness, are displayed in Fig. 8b. It is noted that E_o decreases while E_d increases with enlarging film thickness. This behavior is related to the change in the Atoms diffusion rate in the $CCTS_4$ films, showing an increase in the number of atoms at interstitial cited [39]. The other oscillator parameters for the $CCTS_4$ thin films like the static refractive index, n_o (0), Wemple-DiDomenico energy gap E_g^{wmp} and the static dielectric constant, $\varepsilon_s(= n_o^2)$ have been evaluated according to the presented relations [40–42]:

$$n_0 = \sqrt{1 + \frac{E_d}{E_o}} \quad (11)$$

$$E_g^{wmp} = \frac{E_o}{2} \quad (12)$$

$$\varepsilon_s = n_0^2 \quad (13)$$

Table 3 displayed the oscillator parameters for the $CCTS_4$ films. It is noticed that E_d, n_0, ε_s values boost. Moreover, the values of E_g, E_o, f, E_g^{wmp} were decreased with the increase in film thickness due to the reduction in the energy of the bonds formed between the film elements [43]. It was found that the relation between E_o and E_g follows by this formula $E_o \approx 1.8\ E_g$ which coincides with the anticipation of a single oscillator model.

3.2.5 Optical and electrical conductivities

The optical and electrical conductivities of the $CCTS_4$ films obtained at different thicknesses (160 nm, 230 nm, 297 nm and 345 nm) were determined via the expressions [44, 45]:

Table 4 The E_g values for the different kesterite thin films

Kesterite thin films	Technique	E_g
Cu_2CoSnS_4	Sol gel	1.40 eV [26]
Cu_2ZnSnS_4	Spray pyrolysis	1.40–1.45 eV [29]
Cu_2CdSnS_4	Spray pyrolysis	1.38 -1.49 eV [30]
Cu_2NiSnS_4	Chemical method	1.18 -1.1 eV [31]
Cu_2FeSnS_4	Spray pyrolysis	1.54 -1.76 eV [32]

Table 3 The optical band gap and the values of the dispersion parameters for the $CCTS_4$ thin films

Film thickness (nm)	E_g^{dir}(eV)	E_u (eV)	E_d (eV)	E_o (eV)	n_o	ε_s	f	E_g^{WD} eV
160	1.41	0.74	17.15	3.02	2.58	6.67	51.79	1.51
230	1.21	0.77	17.53	2.76	2.72	7.35	48.38	1.38
297	118	0.79	18.48	2.425	2.93	8.62	44.82	1.22
345	1.12	0.86	19.92	2.135	3.21	10.34	42.52	1.06

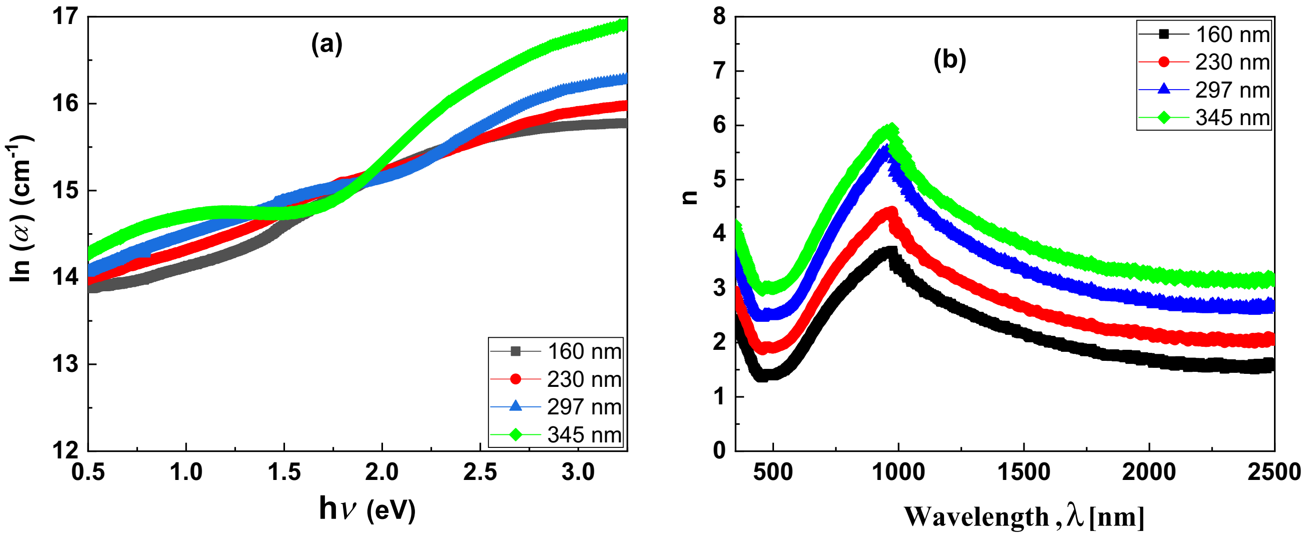

Fig. 7 **a** The variation of the ln (α) with the wavelength for the $CCTS_4$ thin films., **b** The refractive index n as a function of wavelength for the sprayed $CCTS_4$ films under study

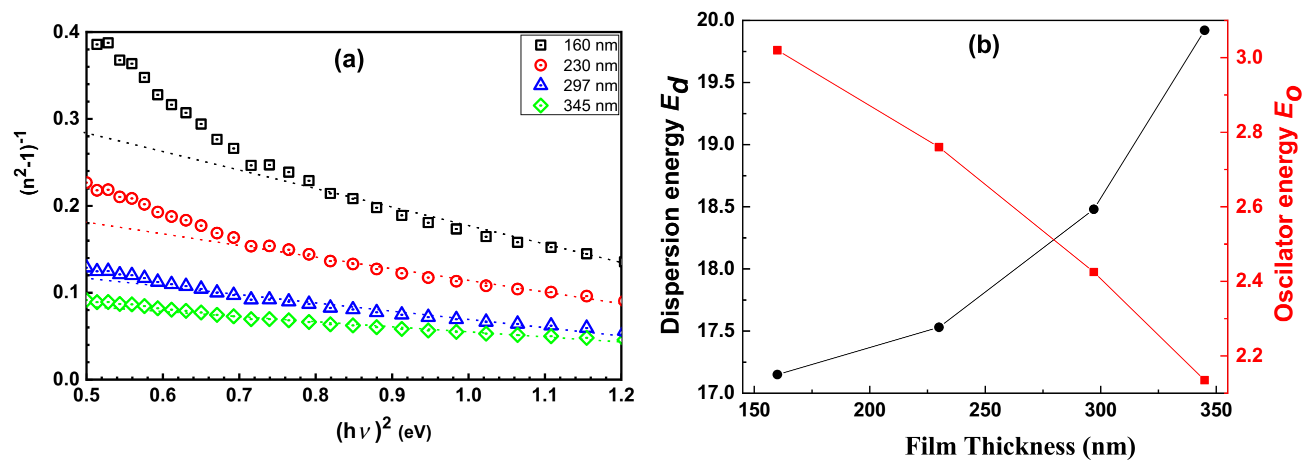

Fig. 8 **a** The dependence of $\left(n^2-1\right)^{-1}$ on $(h\nu)^2$ for the sprayed $CCTS_4$ films, **b** The refractive index n as a function of wavelength for the sprayed $CCTS_4$ films under study

$$\sigma_{\mathrm{opt}} = \frac{\alpha n c}{4\pi} \tag{14}$$

$$\sigma_{\mathrm{e}} = \frac{2\lambda\sigma_{\mathrm{opt}}}{\alpha} \tag{15}$$

Here σ_{opt} denotes the optical conductivity, c presents the speed of light, σ_{e} denotes the electrical conductivity and α implies the absorption coefficient and n refers to the refractive index.

The subordination of optical conductivity on the variation in photon energy for $CCTS_4$ films is presented in Fig. 9a. The analysis of this curve displayed that the optical conductivity of the $CCTS_4$ films boosts with enlarging the film thickness and rising up photon energy. This behavior related to boosting electrons excitation via rising up the incident photon energy, and due to the increase in film absorption coefficients [46]. Figure 9b reveals the reliance of the electrical conductivity on the increase in both photon energy and film thickness for the sprayed $CCTS_4$ thin films. It is clearly seen that electrical conductivity values increase with enlarging film thickness and reduce with the excess in photon energy.

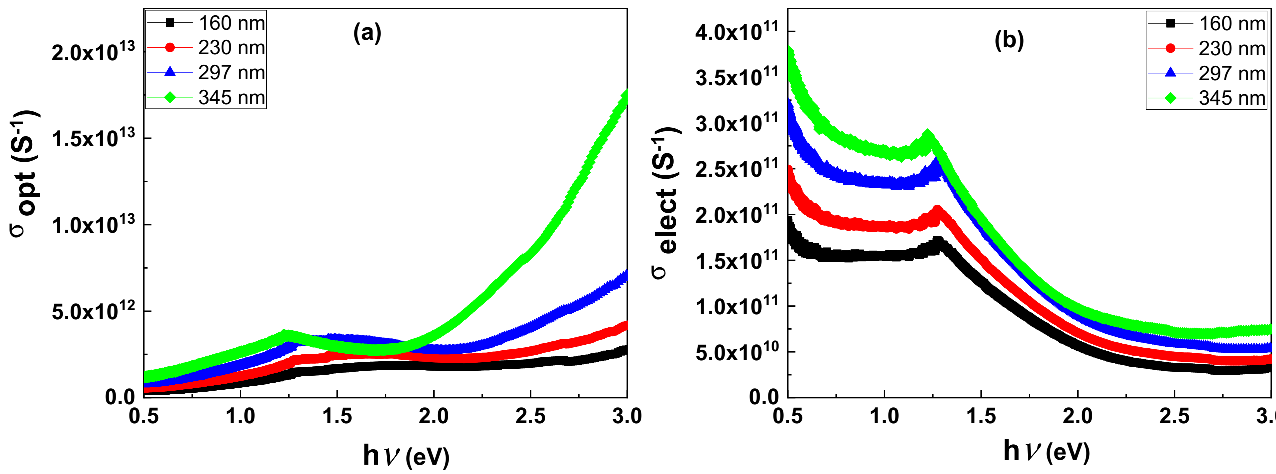

Fig. 9 **a** The dependence of the optical conductivity on the photon energy of the $CCTS_4$ thin films, **b** The electrical conductivity as a function of photon energy for the $CCTS_4$ thin film

3.2.6 Optical dielectric constants

The magnitudes of the dielectric constants of the $CCTS_4$ films synthesized at different thicknesses (160 nm, 230 nm, 297 nm and 345 nm) were evaluated via the relations [47, 48]:

$$\varepsilon_1 = n^2 - k^2 \quad (16)$$

$$\varepsilon_2 = 2nk \quad (17)$$

Here ε_2 denotes the imaginary part of the dielectric constant and the ε_1 implies the real part of dielectric constant for the $CCTS_4$ thin films.

For the $CCTS_4$ films, the subordination of the real and imaginary parts of dielectric constant on the wavelength and the film thickness is presented in Fig. 10a, b. It is noted from these plots that the ε_1 and ε_2 were increased with increasing film thickness. This is expected as both refractive indices and absorption indices values increase with the increase in film thickness and both ε_1 and ε_2 boost as well. Furthermore, the ε_1 trend follows the behavior of films refractive index and ε_2 ensues the trend of film absorption index.

3.3 Nonlinear optical characterization

Investigation of material's nonlinear characteristics is very important where it paves the way for detecting the

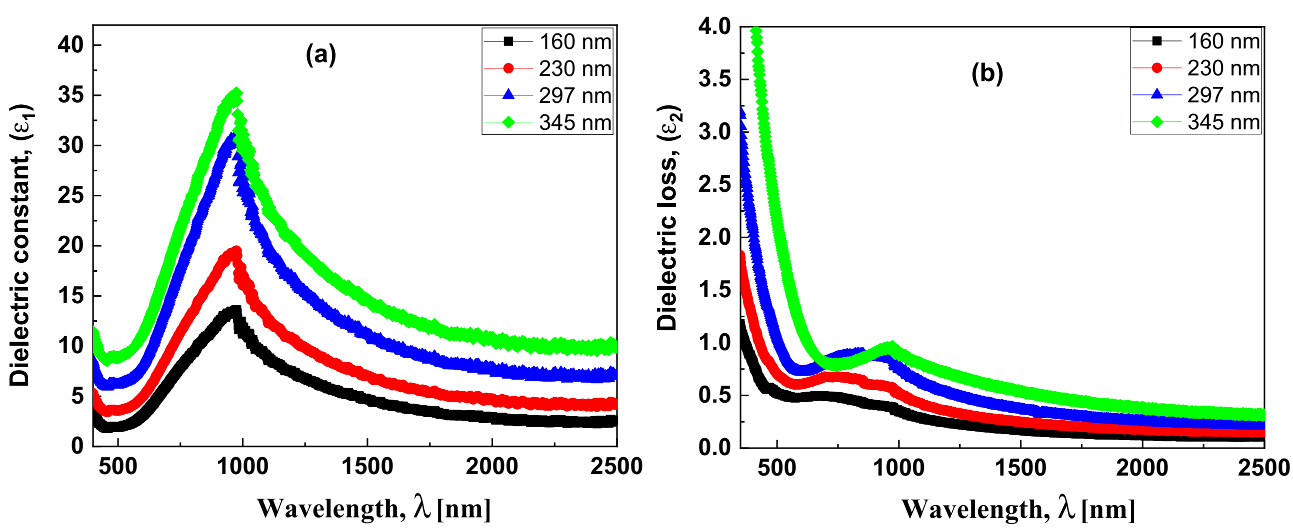

Fig. 10 **a** The dependence of the optical conductivity on the photon energy of the $CCTS_4$ thin films, **b** The electrical conductivity as a function of photon energy for the $CCTS_4$ thin film

Table 5 The nonlinear optical parameters for the $CCTS_4$ thin films

Film thickness (nm)	$\chi^{(3)} \times 10^{-12}$ (esu)	$n_2 \times 10^{-11}$ (esu)
160	0.64	1.18
230	1.16	2.045
297	2.39	3.912
345	4.28	6.591

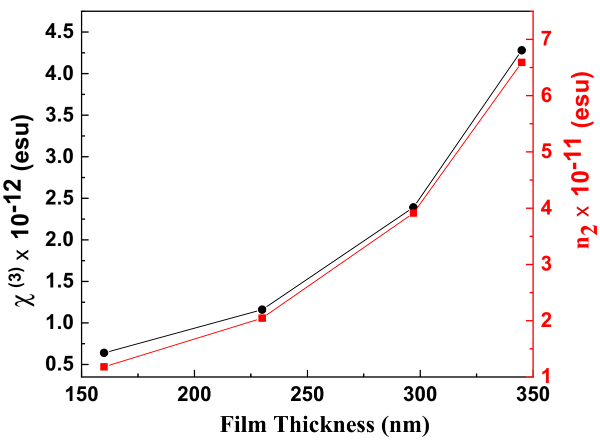

Fig. 11 The dependence of third-order nonlinear optical susceptibility $\chi^{(3)}$ and nonlinear refractive index n_2 on the thickness of the $CCTS_4$ thin films

possibility of exploiting studied materials in various applications such as high capacity communication systems, optical circuits, and photonic applications. The third-order nonlinear optical susceptibility $\chi^{(3)}$ of the $CCTS_4$ films was computed via Miller's principles according to the present formula [49, 50]:

$$\chi^{(3)} = B\left[\frac{{n_0}^2 - 1}{4\pi}\right]^4 \quad (18)$$

Here B is a constant factor equal 1.7×10^{-10} esu and n_0 denotes the values of the static refractive index.

The nonlinear refractive index n_2 of the $CCTS_4$ films is estimated by the expression [51, 52]

$$n_2 = \frac{12\pi\chi^{(3)}}{n_0} \quad (19)$$

Table. 5 displayed the magnitudes of both $\chi^{(3)}$ and n_2 for the $CCTS_4$ thin films. Figure 11 depicted the dependence of the $\chi^{(3)}$ and n_2 on the film thickness. It can be noticed that the $\chi^{(3)}$ and n_2 were raised via increasing the film thickness. This refers to the increase in nonlinear optical properties with the rise in film thickness. This could be referred to the excess of free carriers in the material. The large magnitudes of the obtained nonlinear constants could make our studied material as a good applicant in the fabrication of low power devices for telecommunication applications.

4 Conclusion

In this work, Cu_2CoSnS_4 thin-film samples were fabricated by using the spray pyrolysis method at four various thicknesses (160 nm, 230 nm, 297 nm and 345 nm). The XRD charts of the $CCTS_4$ films depicted that the $CCTS_4$ films are polycrystalline with tetragonal single phase. The EDAX technique displayed that the compositional element ratio was near to 2:1:1:4. The linear optical results displayed that the absorption coefficient of the $CCTS_4$ films was boosted with raising the film thickness while the energy gap has a reverse manner. In addition, the values of the Urbach energy and the optical dielectric constants of the $CCTS_4$ films were computed. Moreover, the nonlinear refractive index n_2, and optical conductivity, of the $CCTS_4$ thin films were raised with increasing film thickness. The increase in nonlinear parameters of $CCTS_4$ films with boosting the film thickness highlights the opportunity of exploiting the studied material in many of interesting optoelectronic devices.

Acknowledgements This work was funded by the Deanship of Scientific Research (DSR) at King Abdulaziz University, Jeddah, under Grant No. J: 91-665-1441. The authors, therefore, acknowledge with thanks DSR for technical and financial support.

References

1. X. Liu, Y. Feng, H. Cui, F. Liu, X. Hao, G. Conibeer, D.B. Mitzi, M. Green, Prog. Photovolt. Res. Appl. **24**, 879 (2016)
2. S. Siebentritt, S. Schorr, Prog. Photovolt. Res. Appl. **20**, 512 (2012)
3. D.B. Mitzi, O. Gunawan, T.K. Todorov, K. Wang, S. Guha, Sol. Energy Mater. Sol. Cells **95**, 1421 (2011)
4. R. Schurr, A. Hölzing, S. Jost, R. Hock, T. Voß, J. Schulze, A. Kirbs, A. Ennaoui, M. Lux-Steiner, A. Weber, I. Kötschau, H.W. Schock, Thin Solid Films **517**, 2511 (2009)
5. S. Chen, A. Walsh, Y. Luo, J.-H. Yang, X.G. Gong, S.-H. Wei, Phys. Rev. B **82**, 195203 (2010)
6. A. Fischereder, T. Rath, W. Haas, H. Amenitsch, J. Albering, D. Meischler, S. Larissegger, M. Edler, R. Saf, F. Hofer, G. Trimmel, Chem. Mater. **22**, 3399 (2010)
7. A. Ziti, B. Hartiti, H. Labrim, S. Fadili, H.J. Tchognia Nkuissi, A. Ridah, M. Tahri, P. Thevenin, Appl. Phys. A: Mater. Sci. Process. **125**, 218 (2019)
8. X. Zeng, K.F. Tai, T. Zhang, C.W.J. Ho, X. Chen, A. Huan, T.C. Sum, L.H. Wong, Sol. Energy Mater. Sol. Cells **124**, 55 (2014)
9. M.S. Kumar, S.P. Madhusudanan, S.K. Batabyal, Sol. Energy Mater. Sol. Cells **185**, 287 (2018)
10. H.I. Elsaeedy, J. Mater. Sci.: Mater. Electron. **30**, 12545 (2019)
11. P.S. Maldar, A.A. Mane, S.S. Nikam, S.D. Giri, A. Sarkar, A.V. Moholkar, J. Mater. Sci.: Mater. Electron. **28**, 18891 (2017)
12. M. Krishnaiah, R.K. Mishra, S.G. Seo, S.H. Jin, J.T. Park, Ceram. Int. **45**, 12399 (2019)

13. P.S. Maldar, M.A. Gaikwad, A.A. Mane, S.S. Nikam, S.P. Desai, S.D. Giri, A. Sarkar, A.V. Moholkar, Sol. Energy **158**, 89 (2017)
14. M. Beraich, M. Taibi, A. Guenbour, A. Zarrouk, M. Boudalia, A. Bellaouchou, M. Tabyaoui, S. Mansouri, Z. Sekkat, M. Fahoume, Optik **193**, 162996 (2019)
15. I.M.H.I. EI RadafElsaeedy, H.A. Yakout, M.T. El Sayed, J. Electron. Mater. **48**, 6480 (2019)
16. A. Sawaby, M.S. Selim, S.Y. Marzouk, M.A. Mostafa, A. Hosny, Phys. B **405**, 3412 (2010)
17. E.R. Shaaban, N. Afify, A. El-Taher, J. Alloys Compd. **482**, 400 (2009)
18. I.M.S.S. El RadafFouad, A.M. Ismail, G.B. Sakr, Mater. Res. Express. **5**, 46406 (2018)
19. C.-J. Kim, I.-S. Ahn, K.-K. Cho, S.-G. Lee, J.-K. Chung, J. Alloys Compd. **449**, 335 (2008)
20. A.S. Hassanien, I. Sharma, J. Alloys Compd. **798**, 750 (2019)
21. T.A. Hameed, I.M. El Radaf, H.E. Elsayed-Ali, J. Mater. Sci.: Mater. Electron. **29**, 12584 (2018)
22. A.S. Hassanien, I. Sharma, Optik **200**, 163415 (2020)
23. I.M. El Radaf, Appl. Phys. A: Mater. Sci. Process. 125 (2019)
24. J. Tauc, R. Grigorovici, A. Vancu, Phys. Status Solidi (B) **15**, 627 (1966)
25. A.S. Hassanien, A.A. Akl, Appl. Phys. A **124**, 752 (2018)
26. A.J. Jebathew, M. Karunakaran, K.D.A. Kumar, S. Valanarasu, V. Ganesh, M. Shkir, I.S. Yahia, H.Y. Zahran, A. Kathalingam, Phys. B **574**, 411674 (2019)
27. I.S. Yahia, I.M.A.M. El RadafSalem, G.B. Sakr, J. Alloys Compd. **776**, 1056 (2019)
28. B. Murali, M. Madhuri, S.B. Krupanidhi, Cryst. Growth Des. **14**, 3685 (2014)
29. L. Nie, S. Liu, Y. Chai, R. Yuan, J. Anal. Appl. Pyrol. **112**, 363 (2015)
30. N. Bitri, S. Dridi, F. Chaabouni, M. Abaab, Mater. Lett. **213**, 31 (2018)
31. S.G. Nilange, N.M. Patil, A.A. Yadav, Phys. B **560**, 103 (2019)
32. Y.B.K. Kumar, G.S. Babu, P.U. Bhaskar, V.S. Raja, Sol. Energy Mater. Sol. Cells **93**, 1230 (2009)
33. T.A. Hameed, A.R. Wassel, I.M. El Radaf, J. Alloys Compd. **805**, 1 (2019)
34. I.M. El Radaf, J. Mater. Sci.: Mater. Electron. **31**, 3228 (2020)
35. T. Wada, T. Maeda, Phys. Status Solidi C **14**, 1600196 (2017)
36. A.S. Hassanien, I.M. El Radaf, Phys. B **585**, 412110 (2020)
37. H.M. Hosni, S.A. Fayek, S.M. El-Sayed, M. Roushdy, M.A. Soliman, Vacuum **81**, 54 (2006)
38. S.H. Wemple, Phys. Rev. B **7**, 3767 (1973)
39. H. Ticha, L. Tichy, J. Optoelectron. Adv. Mater **4**, 381 (2002)
40. A.S. Hassanien, A.A. Akl, Superlattices Microstruct. **89**, 153 (2016)
41. M.M. El-Nahass, A.A.M. Farag, Opt. Laser Technol. **44**, 497 (2012)
42. M. Mohamed, E.R. Shaaban, M.N. Abd-el Salam, A.Y. Abd-elLatief, S.A. Mahmoud, M.A. Abd-elRahim, Optik **178**, 1302–1312 (2019)
43. A.S. Hassanien, A.A. Akl, J. Alloys Compd. **648**, 280 (2015)
44. S.S. Fouad, E.A.A. El-Shazly, M.R. Balboul, S.A. Fayek, M.S. El-Bana, J. Mater. Sci.: Mater. Electron. **17**, 193 (2006)
45. I.M.R.M. El RadafAbdelhameed, J. Alloys Compd. **765**, 1174 (2018)
46. S. Fouad, I.P. El RadafSharma, M. El-Bana, J. Alloys Compd. **757**, 124 (2018)
47. M.S. AlKhalifah, I.M.M.S. El RadafEl-Bana, J. Alloys Compd. **813**, 152169 (2020)
48. S. Hamrouni, M.S. AlKhalifah, M.S. El-Bana, S.K. Zobaidi, S. Belgacem, Appl. Phys. A **124**, 555 (2018)
49. R.M. Abdelhameed, I.M. El Radaf, Mater. Res. Express. **5**(6), 066402 (2018)
50. I.M. El Radaf, T.A. Hameed, G.M. EI komy, T.M. Dahy, Ceram. Int. **45**, 3072–3080 (2019)
51. A.A.A. Darwish, M. Rashad, A.E. Bekheet, M.M. El-Nahass, J. Alloys Compd. **709**, 640 (2017)
52. V. Ganesh, I.S. Yahia, S. AlFaify, M. Shkir, J. Phys. Chem. Solids **100**, 115 (2017)